Dalton Transactions

ROYAL SOCIETY OF CHEMISTRY

PAPER

View Article Online
View Journal | View Issue

Cite this: *Dalton Trans.*, 2024, **53**, 8958

Synthesis of highly luminescent core–shell nanoprobes in a single pot for ofloxacin detection in blood serum and water†

Pallavi Kadian,[a] Astha Singh,[a] Manish Kumar,[b] Kanchan Kumari,[a] Deepika Sharma[a] and Jaspreet Kaur Randhawa *[b]

Antibiotics are commonly used as antibacterial medications due to their extensive and potent therapeutic properties. However, the overconsumption of these chemicals leads to their accumulation in the human body *via* the food chain, amplifying drug resistance and compromising immunity, thus presenting a significant hazard to human health. Antibiotics are classified as organic pollutants. Therefore, it is crucial to conduct research on precise methodologies for detecting antibiotics in many substances, including food, pharmaceutical waste, and biological samples like serum and urine. The methodology described in this research paper introduces an innovative technique for producing nanoparticles using silica as the shell material, iron oxide as the core material, and carbon as the shell dopant. By integrating a carbon-doped silica shell, this substance acquires exceptional fluorescence characteristics and a substantial quantum yield value of 80%. By capitalising on this characteristic of the substance, we have effectively constructed a fluorescent sensor that enables accurate ofloxacin analysis, with a detection limit of 1.3×10^{-6} M and a linear range of concentrations from 0 to 120×10^{-6} M. We also evaluated the potential of CSIONPs for OLF detection in blood serum and tap water analysis. The obtained relative standard deviation values were below 3.5%. The percentage of ofloxacin recovery from blood serum ranged from 95.52% to 103.28%, and from 89.9% to 96.0% from tap water.

Received 21st December 2023,
Accepted 4th March 2024

DOI: 10.1039/d3dt04295b

rsc.li/dalton

Introduction

The rapid progression of antibiotic-microbial resistance (AMR) poses a major and pressing public health dilemma. According to the World Health Organization (WHO), the emergence of antimicrobial resistance (AMR) might lead to around 10 million deaths by the year 2050. The COVID-19 pandemic has led to a rise in the usage of antibiotics in medical settings as a preventive measure against secondary infections, which emphasizes an underlying health concern.[1] Both humans and animals frequently encounter insufficient absorption and metabolism of antibiotics, which increases the risk of the prolonged development and dissemination of antibiotic-resistant genes (ARGs) and bacteria (ARBs), along with adverse effects on the environment and human health.[2,3] Moreover, the extensive utilization of antibiotics leads to the accumulation of these substances in groundwater, animals, humans, and soil.[4–7] Hence it is necessary to develop cutting-edge analytical platforms that are capable of rapid, accurate, and selective antibiotic detection.

Conventional methods for identifying antibiotics include HPLC, chemiluminescence, capillary electrophoresis, flow injection spectrophotometry, use of aptasensors, electrochemical approaches, and fluorescence.[8–12] The latest techniques for sensing include electrochemical and fluorescence approaches.[13–15] Graphene nanocomposites doped with nitrogen and cuprous oxide were utilized by Wu Fanghui *et al.*[16] as electrochemical sensors for detecting ofloxacin (OLF) with a detection limit of 0.34 M. This method has notable constraints, such as poor reproducibility, a lengthy pre-treatment process, and a high threshold for the detection limit (DL).[17] Fluorescence technology, on the other hand, overcomes these limitations in terms of simplicity, fast response time, high sensitivity, real-time sensing, non-destructiveness, and requiring no pre-treatment.[18]

Several recent studies have used molecular imprinting, aptamers, carbon dots, quantum dots (QDs), lanthanide ion integrated metal organic frameworks (MOFs), and covalent organic frameworks (COFs).[9,18–22] In the study by S. B. Aissa *et al.* the Förster Resonance Energy Transfer Mechanism was

[a]*School of Chemical Sciences, Indian Institute of Technology, Mandi, India*
[b]*School of Materials and Mechanical Engineering, Indian Institute of Technology, Mandi, India. E-mail: jaspreet@iitmandi.ac.in*

† Electronic supplementary information (ESI) available. See DOI: https://doi.org/10.1039/d3dt04295b

employed by putting the fluorophore and the quencher together in proximity, and the hybridization of a fluorescein-labeled aptamer (FAM-APT) with a tetramethyl rhodamine-labeled complementary sequence (TAMRA-cDNA) produced maximal fluorescence quenching in the absence of OLF. When the target OLF is introduced, the aptamer changes conformation by producing a FAM-APT/OLF complex, which partially recovers fluorescence under optimal conditions.[23] Z. Yan *et al.* proposed an OLF sensor based on aptamer coated gold nanoparticles and Rhodamine B dye as an amplifier. The detection limit was 4.61×10^{-9} M in a milk sample and 1.66×10^{-9} M in aqueous solution.[24] X. Q. Yao *et al.* use a dual functional sensor based on an MOF to detect OLF and nitroaromatic chemicals.[25] K. Suanchan *et al.* created a polymer nanocomposite comprising graphene QDs and hierarchical porous carbon that was used as a fluorescent probe for OLF sensing with a detection limit of 0.06 g L^{-1}.[9] Advances in nanomaterial engineering techniques have made it easier to integrate two or more independent components into core–shell nanoparticles. The occurrence of several nanostructured phases with different compositions has piqued researchers' interest, with one core phase enveloping the shell. This material's key applications in medicine include multimodal bioimaging, medication targeting, genetic manipulation, biological labelling, bio-diagnostics, and photodynamic treatment.[26–28]

This research presents a novel method for fabricating a core–shell structure using a single-step process. The structure consists of iron oxide nanoparticles enclosed within a carbon-doped silica shell. Prior studies have examined iron oxide nanoparticles that were individually coated with silica and carbon, using a multiple step synthesis route.[29] To our knowledge, no single-step synthesis method for CSIONPs has been reported in the literature. Magnetic iron oxide nanoparticles were chosen due to their ease of separation, non-toxicity, biocompatibility, and low cost, as well as the shell constituents' ability to be easily functionalized with ligands, antibodies, and other capping agents.[30] Furthermore, we chose a carbon doped silica shell due to its unique properties such as effective oxidation barriers and shielding of magnetic core materials from corrosion and fast aggregation.[31]

The core–shell material was created using the solvothermal process, which is a method for synthesizing nanoparticles with the bottom-up approach. In this process, we used ferrocene to supply iron and carbon, TEOS to provide silica, and hydrogen peroxide to facilitate oxidation. These synthesized core–shell CSIONPs were then used to detect OLF, which is a component of fluoroquinolone antibiotics. Fluoroquinolones are the third largest group of antibiotics, comprising approximately 17% of the global market.[22] This antibiotic exhibits a wide range of antibacterial efficacy against both Gram-negative and Gram-positive bacteria.[18] The excessive and unfair use of OLF, due to its antidegradation property, may result in tendon injury and peripheral neuropathy.[32] The CSIONPs demonstrate exceptional selectivity without the need for an incubation period. The optimal detection limit was around 1.3×10^{-6} M. In addition, we evaluated the appropriateness of CSIONPs for immediate analysis in both blood serum and tap water. Advancements in sensitivity and engineering will facilitate the progress of the portable OLF sensor.

Materials

HPLC acetone, tetraethyl orthosilicate (TEOS, reagent grade 98%), ferrocene (98%), sodium chloride (NaCl), potassium chloride (KCl), glycine, urea, magnesium carbonate ($MgCO_3$), calcium carbonate ($CaCO_3$), dimethyl formamide (DMF $\geq$ 99%), ascorbic acid, and 2-methylimidazole were purchased from Sigma Aldrich. Hydrogen peroxide (H_2O_2, 35% in water, TCI), ofloxacin tablets IP 200 mg (OFLOX-200), azithromycin tablets IP 500 mg (Azithral-500), metronidazole tablets IP (FLAGYL-400), paracetamol tablets IP 500 mg (CALPOL 500), diclofenac prolonged release tablets IP (VOVERAN SR75), deionized water (resistivity: 18.2 MΩ), tap water, and blood serum collected from a healthy volunteer were used. All chemicals were used without any further purification.

Synthesis of CSIONPS

0.2 g of ferrocene was taken in 60 mL of acetone and sonicated continuously for 30 min to ensure complete dissolution of ferrocene in acetone followed by the addition of 4.5 mL of hydrogen peroxide dropwise. The mixture was stirred on a magnetic stirrer for 1 hour. Then 0.75 mL of TEOS was added to the mixture and stirred for 5 min. This reaction mixture was transferred to a Teflon autoclave cage and placed in an oven at 220 °C for 48 hours. The reaction mixture was allowed to cool at room temperature. The orange-colored precipitate was separated by centrifugation, washed three times with acetone, and dried overnight in an oven at 40 °C for further use.

The synthesis of the core–shell morphology begins with the oxidation of ferrocene's ferrous ions (Fe^{2+}) to ferric ions (Fe^{3+}) using hydrogen peroxide. This oxidation process results in the formation of iron oxide (Fe_2O_3), which serves as the core material. Simultaneously, water from the hydrogen peroxide reacts with TEOS, gradually converting it into silica. This transformation process occurs gradually due to the low water content, allowing silica to deposit as a shell layer over the hematite nanoparticles.

Moreover, carbon present in the solution is incorporated into the shell structure during synthesis. This inclusion of carbon further enhances the properties of the core–shell nanoparticles.

Characterisation

The morphology and particle size distribution of the CSIONP nanostructure were examined using a NOVA Nano SEM 450 field emission scanning electron microscope (FESEM) at a 10 kV accelerating voltage. Transmission electron microscopy (TEM) images were acquired using a FEI Tecnai electron micro-

scope operated at 200 kV with a LaB_6 filament as the source of electrons for TEM imaging and selected area electron diffraction (SAED). Scanning transmission electron microscopy (STEM) coupled with high angle annular dark field (HAADF) imaging, elemental mapping, and energy dispersive X-ray spectroscopy (EDAX) were conducted using a TECNAI G20 HR-TEM operating at 200 kV. A Rigaku Smart Lab diffractometer was used to record powder X-ray diffraction (PXRD) patterns. The diffraction was performed using CuKα radiation, scanning from 10° to 70° at a scan speed of 2° min^{-1}. The Malvern Zetasizer NanoZS was used to calculate the zeta potential, size, and polydispersity index (PDI) of the supplied sample. For recording X-ray photoelectron spectra (XPS), a VG ESCALAB250 electron spectrometer with monochromatic Al K (1486.6 eV) at 15 kV and 10 mA was employed. The adsorption/desorption isotherms and pore volumes of the adsorbents were determined using nitrogen adsorption–desorption isotherms, measured at 77 K using a Quanta chrome Autosorb 1C Brunauer–Emmett–Teller system. Magnetic force microscopy (MFM) imaging experiments were conducted using a Dimension ICON MFM (Bruker) in tapping mode, with a scanning rate of 0.9 Hz. The phase image was acquired by employing magnetic force microscopy with a 50 nm lift height. Data on fluorescence lifetime was acquired using a Horiba Jobin Yyun Deltaflex-01-NL instrument equipped with a 284 nm laser. In order to ascertain the functional groups, Fourier Transform Infrared Spectroscopy (FTIR) data were acquired using an iS20 Nicolet Assembly from Thermo Fisher Scientific using the ATR mode. The relative quantum yield was calculated using a UV-2600, a SHIMADZU UV-Vis spectrophotometer, and an FS5, an EDINBURGH fluorescence spectrophotometer. Fluorescence analysis was performed on unfiltered materials at 20 °C using a VarianTM Cary Eclipse fluorescence spectrometer (Agilent Technologies, USA) with excitation between 200 and 400 nm (5 nm bandwidth) and emission between 280 and 500 nm (2 nm bandwidth).

Fluorescence detection of ofloxacin

To conduct fluorescence investigations, a sample unit was prepared by combining 100 μL of a stock solution of CSIONPs (2 mg mL^{-1}) in 3 mL DMF. The sample was excited with light at a wavelength of 350 nm and the subsequent emission was detected at a wavelength of 432 nm. In addition to conducting OLF sensing, different concentrations of OLF were injected into the sample unit.

Real time antibiotic analysis in tap water and blood serum

In order to conduct the tests on the samples of human blood serum, one part of human blood serum was mixed with two parts of acetonitrile (in a 1 : 2 ratio) to remove large molecules and proteins. This mixture was then centrifuged for 20 minutes at 10 000 rpm and stored at −20 °C. Subsequently, the material was diluted 100 times to minimize potential matrix influence, following the procedure outlined in a previous study.[33] There is no need for pre-treatment for antibiotic analysis in tap water. Using the standard method of addition, the samples of blood serum and tap water were enhanced with the OLF concentrations. Subsequently, the samples were analyzed utilizing the method for the detection of OLF.

Results and discussion

Morphological analysis

The surface characteristics and dimensions of the CSIONPs were analysed using FESEM. The results demonstrated the formation of uniformly distributed spherical core–shell particles with an average diameter of 280–290 nm, as shown in Fig. 1(a). The dynamic light scattering (DLS) analysis revealed that the hydrodynamic diameter of the CSIONPs was 372 nm. This finding aligns with the particle sizes identified during the SEM analysis. The average PDI derived by DLS was 0.071. The zeta potential of CSIONPs was determined to be −41.6 mV, which matches with the values reported in the literature.[34] The highly negative zeta potential value suggests the existence of negatively charged functional groups on the surface, such as –OH. This is further validated in the subsequent section using FTIR analysis.

The transmission electron microscopy (TEM) image of CSIONPs (Fig. 1(b)) exhibits a characteristic core–shell architecture, consisting of an outer layer of 50 nm thickness and an inner core composed of iron oxide constituents. Several α-Fe_2O_3 particles were observed to be enclosed within the core. This phenomenon may be attributed to the mutual attraction among the constituent particles, which arises from the magnetic properties of the iron oxide nanoparticles. The SAED pattern of CSIONPs demonstrates low crystallinity due to the presence of amorphous silica and carbon in the shell (Fig. 1(c)). Fig. 1(d) shows a STEM-HAADF image of CSIONPs, which demonstrates the core shell structure in a very obvious manner. The distribution of elements within the core shell structure is depicted in Fig. 1(e), which shows an overlay of iron, oxygen, silicon, and carbon. Iron, oxygen, and silicon each has its own individual elemental mapping representations seen in Fig. 1(f–h). The EDAX elemental analysis provided conclusive evidence that carbon, iron, oxygen, and silicon were present in the sample (Fig. 1(i)). The magnetic force microscopy topography image, the phase image, and the phase shift *versus* distance plot can be found in Fig. 1(j–l), respectively. The MFM analysis shows that the magnetic domains are aligned in a uniaxial direction by 18 degrees on magnetization but are disordered on demagnetization which is consistent with the findings described in the literature.[35]

Structural analysis

X-ray diffraction study is used to determine the crystalline structure and lattice characteristics of crystals. The results indicate distinct 2θ diffraction peaks at angles of 24.19°, 33.12°, 35.72°, 40.93°, 49.49°, 54.05°, 62.46°, and 64.07°. These peaks correspond to diffraction planes with Miller indices of (012), (104), (110), (113), (024), (116), (214), and (300) accordingly (Fig. 2(a)). The diffraction peaks observed

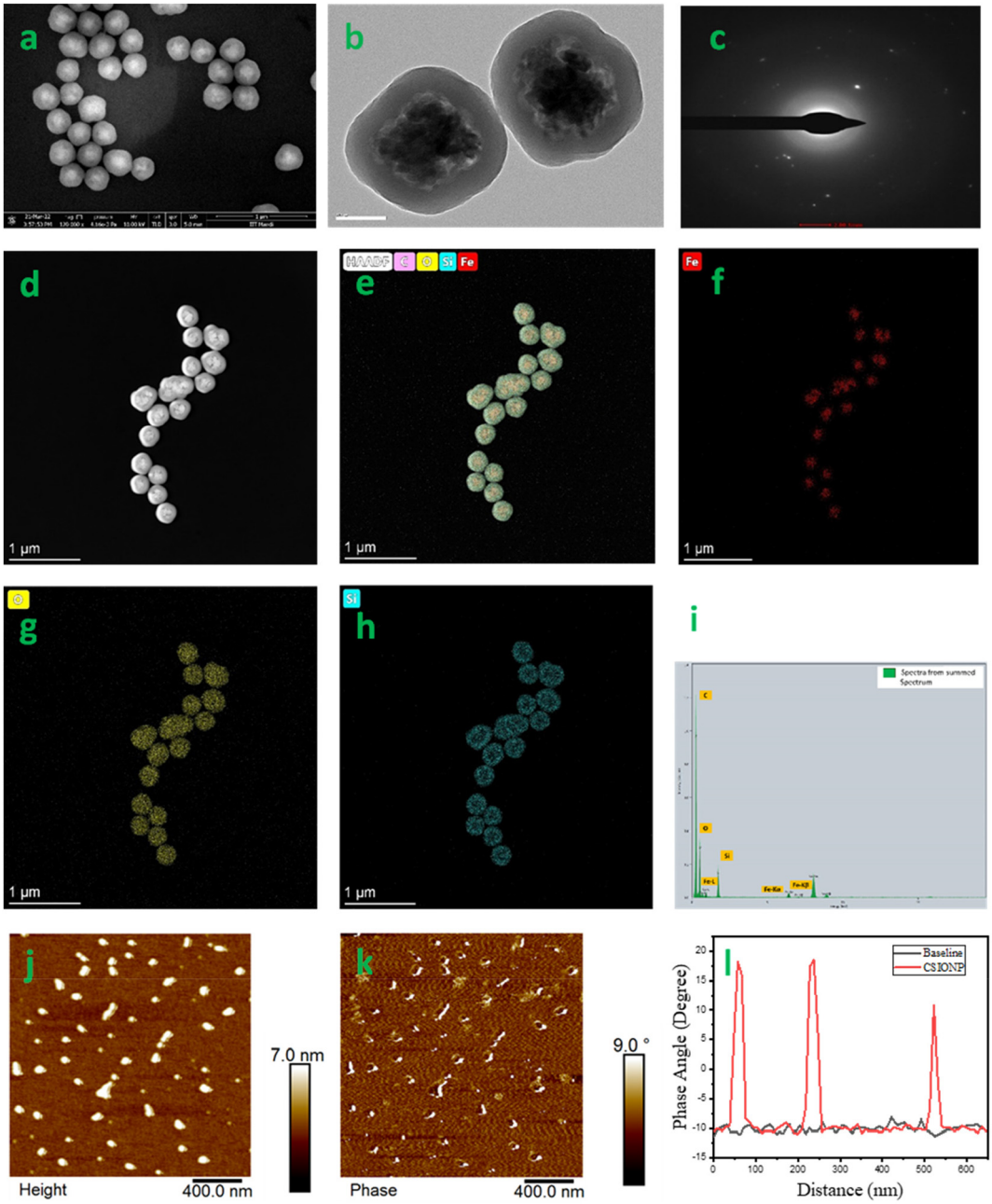

Fig. 1 Morphological analysis: (a) SEM image, (b) TEM image, (c) SAED-HAADF pattern, (d) STEM image (e) overlay of iron, oxygen, silicon and carbon, (f) elemental mapping of iron, (g) elemental mapping of oxygen, (h) elemental mapping of silicon, (i) TEM-EDAX, (j) MFM topographic image, (k) MFM phase shift images, and (l) phase angle *vs.* distance plot of CSIONPs.

were found to be consistent with the rhombohedral crystal structure of hematite (α-Fe_2O_3), as indicated by JCPDS no. 00-024-0072.[36] A broad peak in the 2θ range of 20.0° to 25.0° was observed and this could be attributed to amorphous silica or amorphous carbon.[36,37] The hematite particle's crystallite size was predicted using the Scherrer equation to be around 21.54 nm, which correlated with the greatest intensity peak in the XRD pattern at a Miller index of (104). XPS analysis was used to determine the bond types and oxidation states of the elements. Fig. 2(b) confirms the presence of the elements iron (Fe), silicon (Si), oxygen (O), and carbon (C). Fig. 2(c–f) display deconvoluted high-resolution spectra of iron, silicon, oxygen, and carbon, respectively. The deconvoluted spectra of Fe 2p show peaks with binding energies of 711.16 and 714.60 eV for Fe 2p3/2 and 725.50 eV for Fe 2p1/2.[38,39] The peak observed at 103.80 eV in the silicon deconvoluted spectra is attributed to SiO_2.[40] The deconvoluted oxygen spectrum shows peaks at 531.00 and 533.08 eV, which are respectively assigned to Fe–O and SiO_2.[40,41] The carbon spectra exhibit two well defined peaks at 285.09 and 287.20 eV, which correspond to C–C and

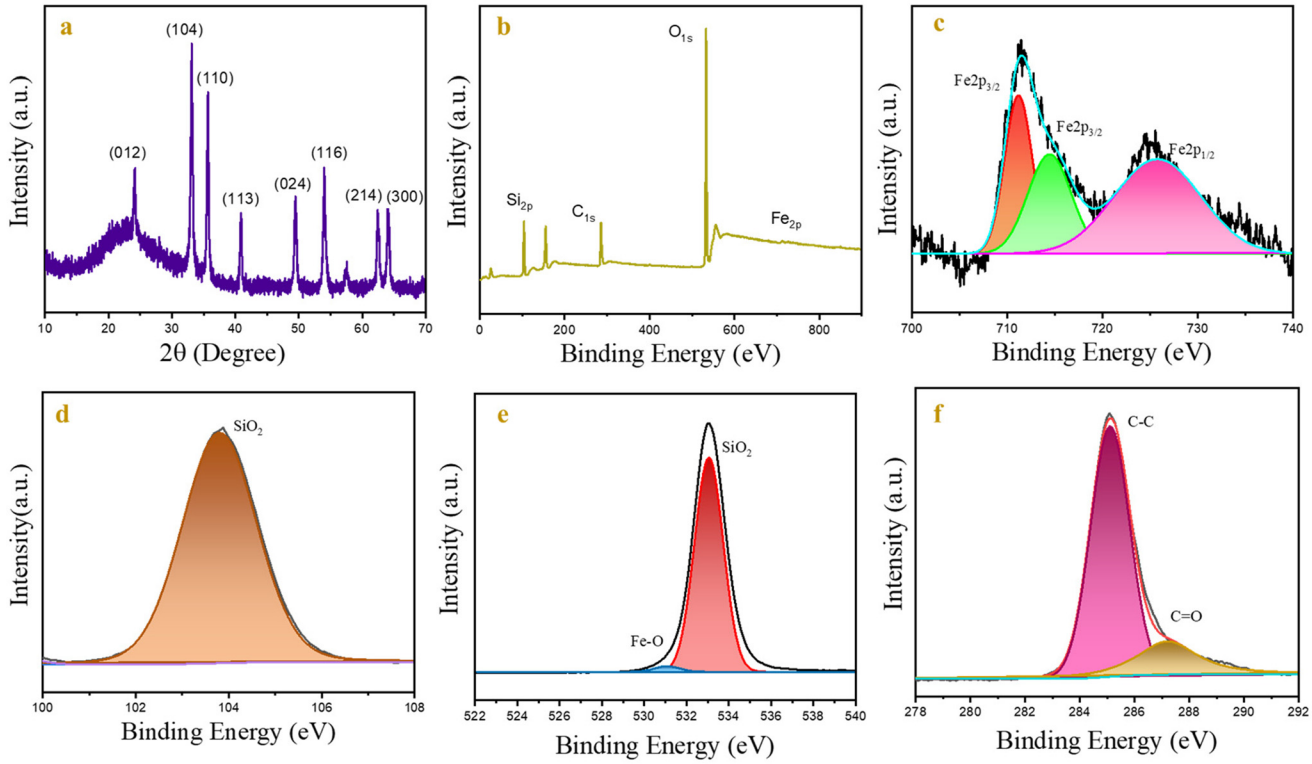

Fig. 2 Structural analysis: (a) XRD pattern, (b) XPS full survey, and (c), (d), (e) and (f) deconvoluted graphs of Fe, Si, O, and C, respectively.

C═O bonds, and these are comparable to those in an earlier report.[39] The carbon source is presumed to be the cyclopentadienyl ligand attached to the ferrocene molecule.

In the FTIR spectra of CSIONPs in Fig. S1,† peaks at 586 cm^{-1} and 634 cm^{-1} represent the stretching frequencies of Fe–O.[42] The peaks at 1045 cm^{-1} and 1128 cm^{-1} are attributed to the symmetric and unsymmetric stretching frequency of the Si–O–Si group.[43] A wide band at 3488 cm^{-1} is attributed to the O–H stretching vibration and the residual adsorbed water. The peak at 1625 cm^{-1} is attributed to the Si–O bond of the silanol group, which is responsible for its hydrophilic nature.[44] A medium peak at 1718 cm^{-1} represents the stretching frequencies of C═O and a weak band at 2348 cm^{-1} is due to the CO_2 adsorbed on the surface. Fig. S2† shows the N_2-adsorption isotherm and pore size distribution of CSIONPs. Using the Brunauer–Emmett–Teller (BET) system, the average pore radius and surface area were found to be 5.92 × 10^{-8} m and 18.535 $m^2\ g^{-1}$, respectively.

Optical properties

The absorption spectrum of CSPIONs in the UV-Vis range is depicted in Fig. 3(a). The spectra exhibit two broad absorption

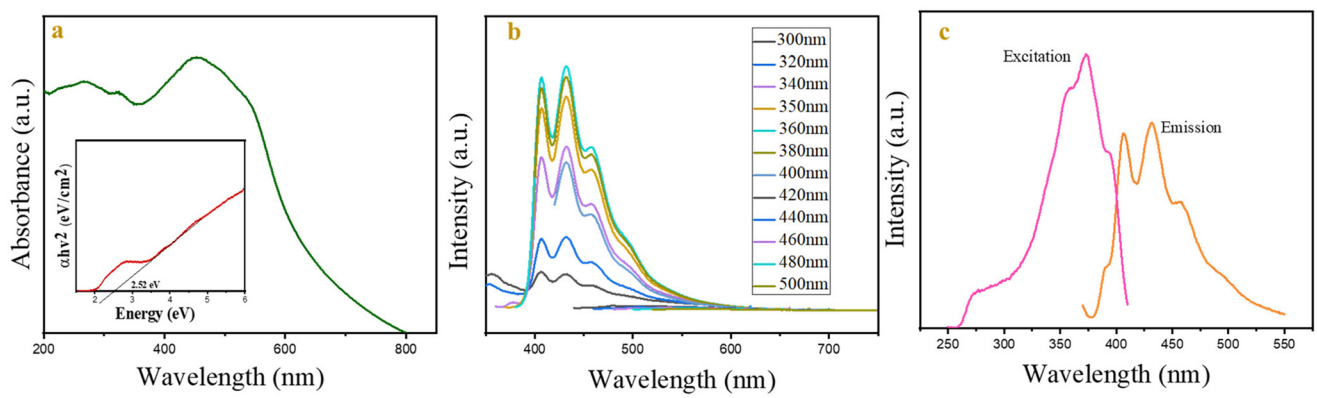

Fig. 3 (a) The UV-Vis spectra of CSIONPs (Tauc plot in the inset), (b) the fluorescence emission spectra of CSIONPs vary under different excitation wavelengths. (c) Excitation and emission spectra of CSIONPs: excitation at 350 nm and emission at 432 nm.

bands spanning the wavelength ranges of 250–410 nm and 420–600 nm. Based on the existing research, the hematite absorption spectra can be divided into four separate segments. Part I (250–400 nm), Part II (400–600 nm), Part III (600–750 nm) and Part IV (750–900 nm). The first part 210–380 nm may result from direct transitions or ligand to metal charge transfer transitions (LMCT), with some contribution from Fe^{3+} ligand field transitions. $^6A_1[6S] \rightarrow {}^4T_1[4P]$ at 290–310 nm and $^6A_1[6S] \rightarrow {}^4E[4D]$ and $^6A_1[6S] \rightarrow {}^4T_1[4D]$ at 360–380 nm, respectively, and pair excitation are responsible for the second absorption from 410 to 550 nm; $^6A_1$ [6S] + $^6A_1[6S] \rightarrow {}^4T_1[4G] + {}^4T_1[4G]$ ligand field transitions had contributed, and were overlapped by $^6A_1[6S] \rightarrow {}^4E$ and $^4A_1[4G]$ ligand field transitions around 430 nm. This transition is what gives hematite its red colour.[45] The fourth zone is often ignored since its absorption coefficients are quite low. SiO_2 did not demonstrate any distinctive absorption band due to its higher refractive index, making it a poor absorber.[36] The Tauc equation governs the material's direct band gap characteristics. As depicted in the inset of Fig. 3(a), the CSIONPs display a direct band gap of 2.52 eV. The absence of photoluminescence (PL) in bulk iron oxide is attributed to thermal and magnetic relaxations.

However, photoluminescence (PL) may arise in nanostructures due to various factors, including the formation of self-trapped states, commonly referred to as the polaronic effect, the quantum confinement effect, and the reduction in hyperfine-field or magnetic interactions.[46] Fluorescence emission spectroscopy and lifetime measurements of CSIONPs were conducted in several solvents, including DI water, acetonitrile, DMF, methanol, and ethanol. Fig. S3 and S4† display the fluorescence emission spectra and decay plots of CSIONPs in various solvents. The computed lifespan of CSIONPs in different solvents is presented in Table S1.† DMF exhibited the most pronounced fluorescence emission intensity and lifetime (0.23 ns). As a result, DMF is used as a solvent in subsequent fluorescence investigations. Fig. 3(b) depicts the emission spectra of CSIONPs in DMF throughout a range of excitation wavelengths (from 300 to 500 nm), with an emission peak at 432 nm. When the excited wavelength varies from 300 to 350 nm, the intensity of emission increases, with the maximum intensity attained at 350 nm and 360 nm. In addition, when the excitation is increased beyond 360 nm, the emission spectra exceed the range and the intensity of emission begins to decrease. The excitation wavelength for fluorescence measurements was selected as 350 nm based on observation. Fig. 3(c) illustrates the excitation and emission spectra of CSIONPs, with the excitation and emission peaks centered at 350 nm and 432 nm, respectively. Fig. S5† displays the fluorescence emission spectra of CSIONPs in the solid state at 350 nm excitation, which indicate that the peaks at 406 nm and 432 nm are the characteristic fluorescence emission peaks of CSIONPs.

Fluorescence stability of CSIONPs

Thermal stability examinations were conducted within the temperature range of 10 to 70 °C. The emission spectra of CSIONPs were determined to be consistently steady within this range (Fig. S6†). The fluorescence stability of CSIONPs at various pH values is studied in a PBS buffer solution of different pH values (3 to 12) (Fig. S7†). The maximum intensity is observed at pH 5. The effect of viscosity on the fluorescence emission spectra of CSIONPs was studied by varying the glycerol composition in a DMF–glycerol mixture (0%, 25%, 50%, 75%, and 100%) (Fig. S8†). The relationship between viscosity and fluorescence emission intensity in mixtures can be complex and may vary depending on the specific components involved. In CSIONPs the observed decrease in fluorescence emission intensity with the increase of viscosity contradicts typical expectations, as mentioned in the existing literature where increased viscosity typically correlates with increased fluorescence emission intensity due to reduced aggregation.[47] However, the experimental data indicate that approximately 93.5% of fluorescence intensity diminishes when viscosity reaches 100%. This significant reduction suggests a strong inverse correlation between viscosity and fluorescence emission intensity in this system. The possible reason may be the inability of CSIONPs to dissolve in non-polar solvents like glycerol.

Fluorescence sensing of ofloxacin

The synthesized CSIONPs were used for the fluorescence sensing of the OLF antibiotic. When OLF was added to the solution of CSIONPs, quenching in the fluorescence peak of the material was observed. Fig. 4(a) shows the change in fluorescence signal intensity with the addition of OLF. At an OLF concentration of 0.3 mM, the fluorescence signal is diminished to about 78%. The Stern–Volmer concept demonstrates the relationship between the fluorescence intensity and OLF levels as follows. The OLF sensing experiment was replicated four times in order to ensure the reproducibility of the results obtained with the sensor.

$$\frac{F_0}{F} = 1 + K(C)$$

where F_0 is the fluorescence intensity of CSIONPs at 432 nm in the absence of OLF; F is the fluorescence intensity of CSIONPs at 432 nm in the presence of OLF; K is the Stern–Volmer constant; and C is the concentration of OLF.

Fig. 4(b) shows the F_0/F *vs.* OLF concentration plot which is linear with an R^2 value of 0.97 and a slope value of 9.11 mM^{-1}. The DL is calculated using the following equation:

$$DL = \frac{(3 \times \sigma)}{S}$$

where, σ is the standard deviation and S is the slope of F_0/F *vs.* OLF concentration

The standard deviation of the fluorescence peak intensity of the material signal was calculated to be 0.4% by performing 10 measurements of CSIONPs with the same concentration and under identical experimental conditions. The detection limit (DL) for OLF was determined to be 1.3×10^{-6} M. The linear range for OLF was from 0 to 120×10^{-6} M. Table 1 dis-

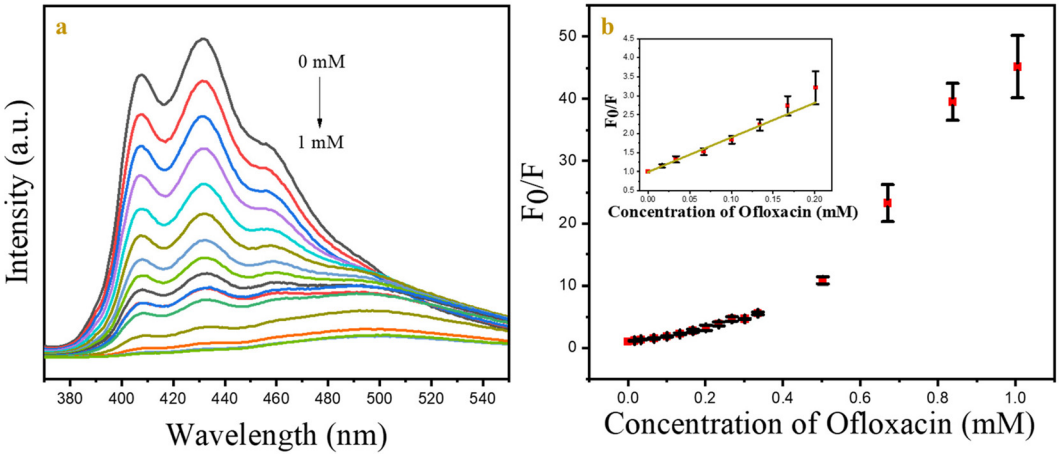

Fig. 4 (a) The emission spectra of CSIONPs were observed in the presence of varying concentrations of OLF. (b) The relationship between F_0/F and the concentration of OLF.

Table 1 Comparison with the reported fluorescent sensors of OLF in the literature

Sensing probe	K_{sv}	Detection limit	Linear range	Ref.
COF-1	—	6.5 μM	0.025×10^{-3}–0.25×10^{-3} M	21
$\{[Zn(TIPA)pim_{0.5}]\ 2H_2O{\cdot}NO_3\}_n$	4.61×10^4 M^{-1}	—	0–40×10^{-6} M	25
FCS-3	1.36×10^5 M^{-1}	0.52 μM	—	48
LnHOFHD film	—	1.2 μM	10^{-3}–10^{-9} M	49
Zn/Eu-MOF	—	0.44 μM	0.1×10^{-6}–80×10^{-6} M	20
CSIONPs	10.9×10^3 M^{-1}	1.3 μM	1×10^{-5}–12×10^{-5} M	This work

plays a comparison examination of our sensor and the sensors referenced in the literature.

The effect of incubation time on quenching behavior was examined using a constant dose of OLF (0.03 mM). Fluorescence emission spectra were collected during time periods ranging from 0 to 60 minutes. Fig. S9† shows a plot of F_0/F as a function of time. Experimental evidence demonstrates that quenching occurs instantly and remains steady for the full hour.

Relative quantum yield

The fluorescence quantum yield for the CSIONPs was estimated using quinine sulphate as a reference. Quinine sulphate shares similar excitation wavelength to the given sample at 350 nm. Quinine sulphate was prepared in 0.1 M H_2SO_4 solution (QY = 0.57, η = 1.33)[50,51] and CSIONPs were dissolved in DMF (η = 1.40).[50] Fig. S10† presents the observed fluorescence spectrum of quinine sulphate and CSIONPs when excited at 350 nm. The following equation was used for the relative quantum yield calculation of the particles based on the standard protocol.

$$\Phi_S = \Phi_R \frac{I_S}{I_R}\left(\frac{1-10^{-A_R}}{1-10^{-A_S}}\right)\left(\frac{n_S}{n_R}\right)^2$$

where Φ_S is the quantum yield of the sample; Φ_R is the quantum yield of quinine sulphate; I_S is the fluorescence intensity of the sample; I_R is the fluorescence intensity of quinine sulphate; A_R is the absorbance of the reference sample; A_S is the absorbance of the sample; n_S is the refractive index of the sample in DMF; and n_R is the refractive index of water.

Observed value from the experiment

$I_S = 295\ 300$ $I_R = 169\ 300$ $A_R = 0.28$ $A_S = 0.34$

The calculated value of quantum yield for CSIONPs was *ca.* 80%.

Mechanism

To determine the mechanism by which CSIONPs sense OFL was studied using time-correlated single photon counting (TCSPC), zeta potential, UV-Vis spectroscopy, and FTIR.

The TCSPC of CSIONPs in DMF shows a lifetime of 0.23 ns which increases to 3.31 ns when OLF is added (Fig. 5(a)). In the case of static quenching, no change in lifespan was seen; however in the event of dynamic quenching, the lifetime may decrease.[52] However, in our instance, we received a boost in lifetime. There could be more than one phenomenon present. The zeta potential of CSIONPs was found to be −41.6 mV when OLF was added to it and the potential value shifted from −41.6 mV to −32.5 mV, which indicated a change in functional groups present on the surface. This finding supports the attachment or adsorption of OLF molecules on the CSIONP surface.

The graphical representation in Fig. 5(b) delineates the absorption spectrum of CSIONP, showcasing a broad peak spanning 200 to 350 nm, further intensifying within the range of 350 to 600 nm. Conversely, OFL exhibits a prominent band

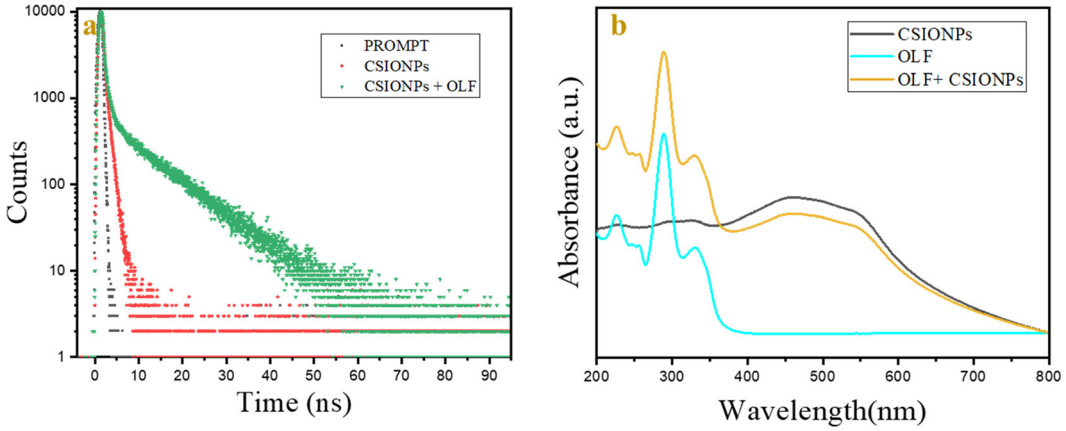

Fig. 5 (a) Lifetime plots of CSIONPs and CSIONPs + OLF and (b) UV-Vis spectra of CSIONPs, OLF and CSIONPs + OLF.

at 290 nm accompanied by two shoulder peaks around 225 nm and 330 nm. The interplay between CSIONS and OFL yields a broad absorption band, reaching the maximum intensity at 290 nm. The reduction in UV absorption intensity is not correlated with the appearance of any new phenomena.[53]

When OLF is added to CSIONPs, the FTIR spectra exhibit three prominent bands. The bands at 3350 cm^{-1}, 1790 cm^{-1} and 1550 cm^{-1} represent the stretching frequencies of O–H, C═O and C═C, respectively, whereas the two bands at 1225 cm^{-1} and 630 cm^{-1} represent the overlapping frequencies of Fe–O and Si–O, respectively[42,43] (Fig. S11(a)†). Because of the overlap of peaks, it is challenging to ascertain the interaction between the CSIONP and OLF. Fig. S11(b)† presents the FTIR spectrum of OLF having peaks at 3400 cm^{-1}, 1609 cm^{-1}, and 1500 cm^{-1} representing OH, COOH and C═C stretching vibrations, respectively.

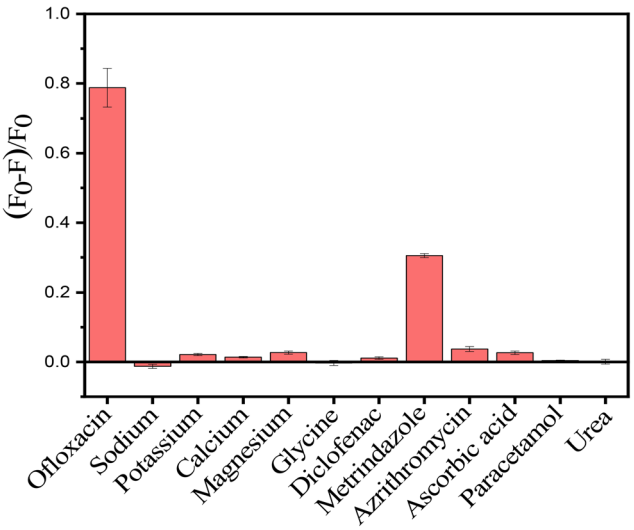

Fig. 6 Selectivity of CSIONPs towards ofloxacin in the presence of a potential interferent.

Selectivity

Selectivity is a key component that can identify a specific analyte target in a mixture without any disturbance of other components present in a complex system. In order to evaluate the selectivity of CSIONPs for OLF, we investigated the impact of various potential interferents, including metal ions such as K^+ and Na^+ (in the form of chloride salts), Mg^{2+} and Ca^{2+} (in the form of carbonate salts), commonly used drugs like azithromycin, diclofenac, paracetamol, and metronidazole, as well as small molecules like urea, glycine, methyl imidazole, and ascorbic acid, on the fluorescence intensity of the CSIONPs. The material exhibited unique and notable variations in fluorescence intensity when exposed to OLF, as seen in Fig. 6. Other substances exhibited minimal impact on the read-out signal. However, metronidazole shows a significant response compared to others. This may be due to the similarity in the structures of these drugs (heterocyclic aromatic ring), or may be the nitro group of metronidazole interacts with CSIONPs, which is common in ofloxacin and metronidazole. The mechanism can be further studied. This demonstrates the exceptionally high selectivity of this sensor towards OLF.

Real sample analysis

To illustrate the practical utility of CSIONPs in sample analysis, we employed the standard addition method with tap water and blood serum. We spiked the tap water with 0.0837, 0.1172 and 0.1507 mM concentration of OLF . The recovery (%) of OLF was in the range of 89.9–96.0% and the relative standard deviation (RSD%) was found to be in the range of 1.24–1.83% (Table 2). Table 3 shows blood serum spiked with 0.0335, 0.1340 and 0.1675 mM concentration of OLF; the calculated recovery (%) of OLF was in the range of 95.52–103.28% and the RSD% was found to be in the range of 1.94–3.12%. Based on these findings, it is evident that the CSIONP sensors produced in this study can be effectively utilised for real sample analysis. The recovery rate and relative standard devi-

Table 2 Detection of OLF in tap water

Sr. no.	OLF added to tap water (mM)	OLF found in tap water (mM)	Recovery (%)	RSD (%)
1.	0.0837	0.0784	93.61	1.24
		0.0804	96.00	
		0.0789	94.20	
2.	0.1172	0.1076	91.76	1.82
		0.1116	95.18	
		0.1109	94.58	
3.	0.1507	0.1356	89.95	1.83
		0.1369	90.81	
		0.1409	93.46	

Table 3 Detection of OLF in blood serum

Sr. no.	OLF added to blood serum (mM)	OLF found in blood serum (mM)	Recovery (%)	RSD (%)
1.	0.0335	0.0333	99.40	1.94
		0.0320	95.52	
		0.0327	97.61	
2.	0.1340	0.1306	97.46	2.60
		0.1372	102.38	
		0.1319	98.43	
3.	0.1675	0.1636	97.67	3.12
		0.1723	102.86	
		0.1730	103.28	

ation (RSD) can indicate the accuracy and consistency of the sensor design. Table S2† presents the recorded percentage of ofloxacin retrieval in water and blood serum, as reported in the literature. The recovery rate may vary from 100% due to the cumulative interference of interferents present in the matrix.[54] Fig. S12† shows OLF detection in tap water and blood serum using CSIONPs, respectively. The recovery (%) was calculated using the given formula

$$\text{Recovery } (\%) = (C_{\text{experimental}}/C_{\text{actual}}) \times 100$$

where $C_{\text{experimental}}$ is the concentration of OLF calculated experimentally and C_{actual} is the spiked concentration of OLF.

Conclusion

Innovative approaches are being developed to improve the efficacy of engineered nanoparticles (CSIONPs). Here, we provide an innovative and efficient method for producing nanoparticles with a core–shell structure, consisting of iron oxide coated with silica and doped with carbon. Significantly, our methodology eliminates the need for surfactants and is accomplished in a single step. The synthesis and characterization of mesoporous carbon-doped silica-coated iron oxide nanoparticles were successfully achieved. The CSIONPs exhibit excellent water dispersibility and colloidal stability, and possess inherent fluorescence with an exceptionally high quantum yield of 80%. This material is being utilized for the first time as a sensor for OLF, exhibiting a high level of selectivity without requiring any incubation period. In the absence of aptamers, a reliable detection limit (DL) of *ca.* 1.3×10^{-6} M was achieved. We also tested the potential of CSIONPs for real sample analysis in tap water and blood serum. The recovery (%) of OLF was in the ranges of 89.9–96.0% and 95.52–103.28% and the relative standard deviation (RSD%) was found to be 1.24–1.83% and 1.94–3.12% for tap water and blood serum, respectively. The lack of the matrix effect indicates that the fluorescent probe is suitable for analyzing real OLF samples. We expect that these findings will soon aid in the development of a significant portable OLF detection sensor that will be advantageous to society.

Ethical statement

The experiments were carried out in compliance with institutional guidelines, and authorized by the Institutional Human Ethics Committee at the Indian Institute of Technology, Mandi (IIT Mandi), Himachal Pradesh, India, with the application number IITM/IEC(H)/2024/JR/P1. Written informed consent was acquired from individuals involved in the present research. We collected the samples from healthy individuals who were not receiving any medications.

Author contributions

Pallavi Kadian carried out the experiment, analyzed the findings, and wrote the manuscript. Astha Singh carried out the lifetime experiments and examined the lifetime data. Manish Kumar analyzed the findings and reviewed the manuscript. Kanchan Kumari and Deepika Sharma performed real sample analysis experiments. Jaspreet Kaur Randhawa conceptualized the project and reviewed the manuscript.

Conflicts of interest

No conflicts of interest to declare.

Acknowledgements

The authors are grateful to AMRC-IIT Mandi for providing characterization facilities and MHRD for providing a research fellowship.

References

1 T. Pulingam, *et al.*, Antimicrobial resistance: Prevalence, economic burden, mechanisms of resistance and strategies to overcome, *Eur. J. Pharm. Sci.*, 2022, **170**, 106103.
2 X. D. Zhu, *et al.*, Fluorescent Metal-Organic Framework (MOF) as a Highly Sensitive and Quickly Responsive Chemical Sensor for the Detection of Antibiotics in Simulated Wastewater, *Inorg. Chem.*, 2018, **57**, 1060–1065.

3 D. Lu, *et al.*, Ionic Liquid-Functionalized Magnetic Metal-Organic Framework Nanocomposites for Efficient Extraction and Sensitive Detection of Fluoroquinolone Antibiotics in Environmental Water, *ACS Appl. Mater. Interfaces*, 2021, **13**, 5357–5367.
4 F. Luan, *et al.*, Facile synthesis of a cyclodextrin-metal organic framework decorated with Ketjen Black and platinum nanoparticles and its application in the electrochemical detection of ofloxacin, *Analyst*, 2020, **145**, 1943–1949.
5 W. Lu, *et al.*, Bright Yellow Fluorescent Carbon Dots as a Multifunctional Sensing Platform for the Label-Free Detection of Fluoroquinolones and Histidine, *ACS Appl. Mater. Interfaces*, 2018, **10**, 42915–42924.
6 A. Kundu, B. Maity and S. Basu, Rice Husk-Derived Carbon Quantum Dots-Based Dual-Mode Nanoprobe for Selective and Sensitive Detection of Fe3+ and Fluoroquinolones, *ACS Biomater. Sci. Eng.*, 2022, **8**, 4764–4776.
7 C. Liu, B. Li, M. Liu and S. Mao, Demand, status, and prospect of antibiotics detection in the environment, *Sens. Actuators, B*, 2022, **369**, 132383.
8 N. Lian, Y. Zhang, D. Liu, J. Tang and H. Wu, Copper nanoclusters as a turn-on fluorescent probe for sensitive and selective detection of quinolones, *Microchem. J.*, 2021, **164**, 105989.
9 K. Suanchan, N. Chansud, S. Sa-nguanprang and O. Bunkoed, A nanocomposite optosensing probe based on hierarchical porous carbon and graphene quantum dots incorporated in selective polymer for the detection of trace ofloxacin, *Colloids Surf., A*, 2021, **628**, 127376.
10 P. S. Francis and J. L. Adcock, Chemiluminescence methods for the determination of ofloxacin, *Anal. Chim. Acta*, 2005, **541**, 3–12.
11 R. Aggarwal, *et al.*, Cellulose-Derived Carbon Dots for Inner Filter Effect-Based Selective Sensing of Ofloxacin Antibiotics, *ACS Appl. Nano Mater.*, 2023, **6**, 6518–6527.
12 Q. Li, *et al.*, Molecular-level enhanced clusterization-triggered emission of nonconventional luminophores in dilute aqueous solution, *Nat. Commun.*, 2023, **14**, 409.
13 Y. Chen, *et al.*, Design of 2D/2D CoAl LDH/g-C3N4 heterojunction-driven signal amplification: Fabrication and assay for photoelectrochemical aptasensor of ofloxacin, *Sens. Actuators, B*, 2022, **353**, 131187.
14 X. Si, Y. Wei, C. Wang, L. Li and Y. Ding, A sensitive electrochemical sensor for ofloxacin based on a graphene/zinc oxide composite film, *Anal. Methods*, 2018, **10**, 1961–1967.
15 X. Zhou, *et al.*, Colorimetric determination of ofloxacin using unmodified aptamers and the aggregation of gold nanoparticles, *Microchim. Acta*, 2018, **185**, 355.
16 F. Wu, *et al.*, Cuprous oxide/nitrogen-doped graphene nanocomposites as electrochemical sensors for ofloxacin determination, *Chem. Res. Chin. Univ.*, 2016, **32**, 468–473.
17 Q. Sun, *et al.*, Construction of biomass carbon dots@molecularly imprinted polymer fluorescent sensor array for accurate identification of 5-nitroimidazole antibiotics, *Sens. Actuators, B*, 2022, **373**, 132716.
18 Y. Q. Wang, Z. Fang, H. Min, X. Y. Xu and Y. Li, Sensitive Determination of Ofloxacin by Molecularly Imprinted Polymers Containing Ionic Liquid Functionalized Carbon Quantum Dots and Europium Ion, *ACS Appl. Nano Mater.*, 2022, **5**, 8467–8474.
19 H. Yi, *et al.*, Fluorometric determination for ofloxacin by using an aptamer and SYBR Green I, *Microchim. Acta*, 2019, **186**, 668.
20 Y. Wu, *et al.*, A novel Zn/Eu-MOF for the highly sensitive, reversible and visualized sensing of ofloxacin residues in pork, beef and fish, *Food Chem.*, 2023, **422**, 136250.
21 N. Zhao, *et al.*, Easy Green Construction of a Universal Sensing Platform Based on Crystalline Polyimide Covalent Organic Frameworks with Sensitive Fluorescence Response to Metal Ions and Antibiotics, *ACS Appl. Bio Mater.*, 2021, **4**, 995–1002.
22 X. Wang, *et al.*, Discriminative and quantitative color-coding analysis of fluoroquinolones with dual-emitting lanthanide metal-organic frameworks, *Sens. Actuators, B*, 2022, **373**, 132701.
23 S. B. Aissa, M. Mastouri, G. Catanante, N. Raouafi and J. L. Marty, Investigation of a truncated aptamer for ofloxacin detection using a rapid FRET-based apta-assay, *Antibiotics*, 2020, **9**, 1–16.
24 Z. Yan, *et al.*, Fluorescent aptasensor for ofloxacin detection based on the aggregation of gold nanoparticles and its effect on quenching the fluorescence of Rhodamine B, *Spectrochim. Acta, Part A*, 2019, **221**, 117203.
25 X. Q. Yao, *et al.*, Two triphenylamine-based luminescent metal-organic frameworks as a dual-functional sensor for the detection of nitroaromatic compounds and ofloxacin antibiotic, *CrystEngComm*, 2019, **21**, 2559–2570.
26 K. Chatterjee, S. Sarkar, K. Jagajjanani Rao and S. Paria, Core/shell nanoparticles in biomedical applications, *Adv. Colloid Interface Sci.*, 2014, **209**, 8–39.
27 R. Jenjob, T. Phakkeeree and D. Crespy, Core–shell particles for drug-delivery, bioimaging, sensing, and tissue engineering, *Biomater. Sci.*, 2020, **8**, 2756–2770.
28 Y.-K. Hou, *et al.*, Remodeling the Tumor Microenvironment with Core–Shell Nanosensitizer Featuring Dual-Modal Imaging and Multimodal Therapy for Breast Cancer, *ACS Appl. Mater. Interfaces*, 2023, **15**, 2602–2616.
29 N. Zhu, *et al.*, Surface modification of magnetic iron oxide nanoparticles, *Nanomaterials*, 2018, **8**(10), 810.
30 W. Wu, C. Z. Jiang and V. A. L. Roy, Designed synthesis and surface engineering strategies of magnetic iron oxide nanoparticles for biomedical applications, *Nanoscale*, 2016, **8**, 19421–19474.
31 H. Bae, *et al.*, Carbon-Coated Iron Oxide Nanoparticles as Contrast Agents in Magnetic Resonance Imaging, *Nanoscale Res. Lett.*, 2012, **7**, 44.
32 T. Wu, *et al.*, Dual Direct Z-Scheme Heterojunction with Stable Electron Supply to a Au/PANI Photocathode for Ultrasensitive Photoelectrochemical and Electrochromic Visualization Detection of Ofloxacin in a Microfluidic Sensing Platform, *Anal. Chem.*, 2023, **95**, 1627–1634.

33 A. Tiwari, *et al.*, High quantum yield carbon dots and nitrogen-doped carbon dots as fluorescent probes for spectroscopic dopamine detection in human serum, *J. Mater. Chem. B*, 2022, **11**, 1029–1043.
34 M. Mahmoudi, S. Sant, B. Wang, S. Laurent and T. Sen, Superparamagnetic iron oxide nanoparticles (SPIONs): Development, surface modification and applications in chemotherapy, *Adv. Drug Delivery Rev.*, 2011, **63**, 24–46.
35 S. I. Eguía-Eguía, *et al.*, Magnetic domains orientation in (Fe3O4/γ-Fe2O3) nanoparticles coated by Gadolinium-diethylenetriaminepentaacetic acid (Gd3+-DTPA), *Nano Express*, 2021, **2**, 020019.
36 X. Zhang, Y. Niu, Y. Li, Y. Li and J. Zhao, Preparation and thermal stability of the spindle α-Fe 2O3@SiO_2 core-shell nanoparticles, *J. Solid State Chem.*, 2014, **211**, 69–74.
37 A. Tiwari, N. C. Verma, A. Singh, C. K. Nandi and J. K. Randhawa, Carbon coated core-shell multifunctional fluorescent SPIONs, *Nanoscale*, 2018, **10**, 10389–10394.
38 W. Ge, X. Zhang, X. Ge and K. Liu, Synthesis of α-Fe2O3/SiO_2 nanocomposites for the enhancement of acetone sensing performance, *Mater. Res. Bull.*, 2021, **141**, 111379.
39 S. Li, *et al.*, A nanoarchitectured Na6Fe5(SO4)8/CNTs cathode for building a low-cost 3.6 V sodium-ion full battery with superior sodium storage, *J. Mater. Chem. A*, 2019, **7**, 14656–14669.
40 A. Sakthisabarimoorthi, S. A. Martin Britto Dhas and M. Jose, Fabrication of monodispersed α-Fe2O3@SiO_2 core-shell nanospheres and investigation of their dielectric behavior, *J. Alloys Compd.*, 2019, **771**, 1–8.
41 M. Kumar, A. Tiwari and J. K. Randhawa, Electrospun nanofibers of α-hematite/polyacrylonitrile/calcium carbonate/cellulose triacetate as a multifunctional platform in, wastewater treatment and remineralisation, *Desalination*, 2022, **541**, 116030.
42 S. Hwang, A. Umar, G. N. Dar, S. Kim and R. Badran, Synthesis and Characterization of Iron Oxide Nanoparticles for Phenyl Hydrazine Sensor Applications, *Sens. Lett.*, 2014, **12**, 1–5.
43 J. Sulejmanović, M. Memić, J. Huremovic and A. Selović, Simultaneous Preconcentration and Determination of Co (II), Cr(III), Fe(III), Mn(II), Ni(II) and Pb(II) by FAAS using Silica Gel Modified with Niobium(V) oxide, *Chem. Sci. Rev. Lett.*, 2015, **4**, 662–670.
44 P. Wagh, *et al.*, Hydrophobicity Measurement Studies of Silica Aerogels using FTIR Spectroscopy, Weight Difference Method, Contact Angle Method and K-F Titration Method, *J. Chem., Biol. Phys. Sci.*, 2015, **5**, 2350–2359.
45 A. Sunny, N. Prasad, D. Subbaiyan, S. Dillibabu and K. Balasubramanian, Optical, vibrational and fiber optic gas-sensing properties of hematite microparticles, *Appl. Phys. A: Mater. Sci. Process.*, 2018, **124**, 677.
46 Y. Y. Xu, *et al.*, Synthesis and characterization of single-crystalline α-Fe2O3 nanoleaves, *Phys. E*, 2009, **41**, 806–811.
47 Y. F. Wang, *et al.*, Multi-stable fluorescent silica nanoparticles obtained from in situ doping with aggregation-induced emission molecules, *J. Mater. Chem. B*, 2015, **3**, 8775–8781.
48 C. P. Li, *et al.*, Anionic metal-organic framework as a unique turn-on fluorescent chemical sensor for ultra-sensitive detection of antibiotics, *Chem. Commun.*, 2020, **56**, 12403–12406.
49 X. Xu, J. Wang and B. Yan, Facile Fabrication of Luminescent Eu(III) Functionalized HOF Hydrogel Film with Multifunctionalities: Quinolones Fluorescent Sensor and Anticounterfeiting Platform, *Adv. Funct. Mater.*, 2021, **31**, 2103321.
50 A. Bhatta, *et al.*, Modulated photophysical properties and sequestration of potent anti-acetylcholinesterase active coumarinyl dyes in human serum albumin, *Dyes Pigm.*, 2023, **208**, 110871.
51 Instrumentation for Fluorescence Spectroscopy, in *Principles of Fluorescence Spectroscopy*, ed. J. R. Lakowicz, Springer US, Boston, MA, 2006, pp. 27–61.
52 J. R. Lakowicz, Quenching of Fluorescence, in *Principles of Fluorescence Spectroscopy*, ed. J. R. Lakowicz, Springer US, Boston, MA, 1983, pp. 257–301.
53 J. Zhao, *et al.*, Detection of metronidazole in honey and metronidazole tablets using carbon dots-based sensor via the inner filter effect, *Luminescence*, 2018, **33**, 704–712.
54 Q. Wang, *et al.*, Recent advances in electrochemical sensors for antibiotics and their applications, *Chin. Chem. Lett.*, 2021, **32**, 609–619.